Macromolecules

ARTICLE

pubs.acs.org/Macromolecules

Impact of Out-of-Plane Translational Order in Block Copolymer Lithography

Joan K. Bosworth, Elizabeth A. Dobisz, Olav Hellwig, and Ricardo Ruiz*

San Jose Research Center, Hitachi Global Storage Technologies, 3403 Yerba Buena Rd., San Jose, California 95135, United States

ABSTRACT: In block copolymer lithography, subtle distortions in the self-assembled domains, such as tilting or bending, have a strong impact on the quality of the lithographic features upon pattern transfer. We compared the feature size distribution observed at the top-surface of block copolymer thin films with the size distribution that the self-assembled structures project at the substrate interface, i.e., the lithographic image. We performed the comparison for films of perpendicularly oriented cylindrical block copolymer domains with various degrees of lateral order. We found that the size distribution of the projected image does not mimic the well-known Gaussian distribution observed at the top surface. Instead, the lithographic features display a skewed distribution with a long tail toward smaller feature dimensions, a shift of the median and a reduced number of transferred features. The distortions are more pronounced for films with shorter correlation lengths. We propose a simplified model that explains the observed shifts in the size distribution of the projected image by considering the tilting that cylinders undergo in the vicinity of dislocations. The presence of defects disrupting the in-plane orientational order not only impacts the size distribution of the self-assembled features, but also induces nearby cylinder tilting and some general loss of out-of-plane translational order which, upon pattern transfer, is responsible for the observed distortions on the feature size distribution.

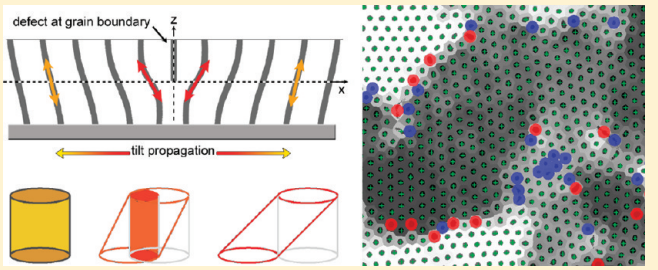

I. INTRODUCTION

Block copolymer lithography has emerged as a promising alternative to reach resolutions not accessible by optical lithography.[1,2] Because of the free energy minimization of the self-assembling process, block copolymer patterns display a high degree of uniformity in both feature size and feature spacing that may not be attainable by any other lithographic technique for sub-20 nm lithography.[3,4] This superior uniformity is the driving force in current efforts to introduce block copolymer lithography into the manufacturing of magnetic bit patterned media (BPM) for data storage and into the International Technology Roadmap for Semiconductors (ITRS).[5] Feature size uniformity is an essential metric in the specifications needed in leading nanolithography applications such as BPM[6−8] and semiconductor devices.[9,10]

A lithographic mask is typically a polymeric resist layer (or, in this case, a block copolymer film) that masks or protects the substrate in certain regions and leaves it exposed in other regions. The fabrication may follow with an additive process (one that adds another material onto the exposed portions of the substrate) or a subtractive one (by removing material from the exposed areas of the substrate). In either case, the openings through the mask project a two-dimensional image at the substrate interface. The size uniformity of the final transferred features depends not only on the uniformity of the features as observed at the top surface, but also on the uniformity of the vertical profile of the mask throughout its thickness. Figure 1 shows a cartoon with examples of cylindrical openings in a resist with varying degrees of uniformity throughout the film. The first cartoon in Figure 1 shows a feature with a perfect vertical profile that preserves its uniformity from top to bottom, meaning that the circular shape on the $x-y$ plane is identical at any level on the z axis throughout the thickness of the film. The projected image at the substrate interface is therefore identical to the top-surface image. On the other hand, if the translational order of the two-dimensional cross section is not preserved throughout the thickness of the film, the projected image is reduced in size due to either tilting or wall roughness. Technically, a tilted cylinder has an ellipsoidal top-surface image, but for small angles, this ellipsoidal shape is difficult to appreciate and can look much like a circle to the unaided eye. However, even for small tilting angles, a non-negligible reduction in the size of the projected image can be observed. The tilted cylinder in Figure 1 was generated by software using a tilting angle of 11° and a cylinder height equal to its diameter.

Size uniformity of block copolymer domains in thin films has been studied extensively, in particular with a focus on measurements from the top air interface.[11−16] Guarini et al observed for block copolymers with perpendicular cylinders that feature size distributions follow a Gaussian distribution, with decreasing standard deviation for longer thermal annealing time and higher annealing temperature.[11] Likewise, Hammond et al observed a broadening of feature size distributions induced by defects, which occur primarily at domain grain boundaries. Here the term grain

Received: August 27, 2011
Revised: October 19, 2011
Published: November 04, 2011

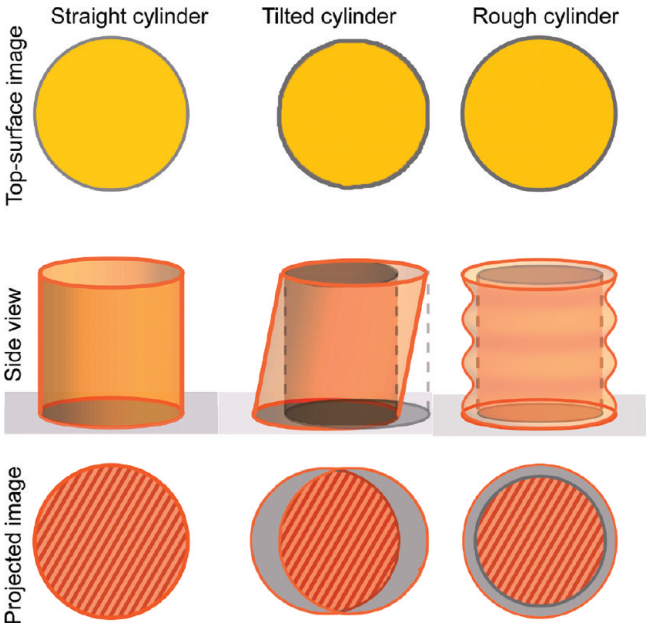

Figure 1. Representation of the difference between feature sizes at the top-surface and at the projected image on the substrate interface for vertical, tilted and rough cylinders. Any loss in translational order in the direction out-of-plane results in a diminished feature size of the projected image.

is defined as a crystallite structure formed by an ordered array of polymer domains in a block copolymer film — in this case, with perpendicularly oriented cylinders packed into a hexagonal lattice such that each dot has six nearest neighbors.[12] Defects at the grain boundaries display features with five and seven nearest neighbors, which, as seen from the top surface, also display distortions to their size and shape. Though these members with five and seven nearest neighbors make up only a small fraction of the total number of features, their distortions have been reported to contribute to an overall broadening of the feature size distribution by adding small satellite peaks on each side of the Gaussian distribution.[12] The distortions around members with five and seven nearest neighbors have been previously explained with a two-dimensional model that captures the deformations as seen on the top surface. We build on these past observations to show that in order to understand the size distribution of the projected lithographic image at the bottom of the film, it is necessary to think of these films as three-dimensional with cylinder tilting around the defect cores.

Here we demonstrate that in thin films of cylindrical-phase block copolymers with perpendicular orientation, the uniformity of the two-dimensional projected image stems not only from the uniformity of the cylinder core itself, but—perhaps more importantly—also from the uniformity of its orientation and translation along the surface normal. The same defects that induce five and seven nearest neighbor spacing in films, namely dislocations, disclinations or grain boundaries, also induce deformations in the cylinder cores, causing variation in their cross sectional areas[12] or deviation in their orientation normal to the surface.[17] In turn, these perturbations can propagate to the neighbors over some distance. This implies that the size uniformity of features defined by block copolymer lithography can be correlated with the lateral correlation length, ξ, albeit with a larger impact on feature size distribution than would be expected for a two-dimensional film for which the top-surface and the projected image would be identical. Here, we compare the feature size distributions both at the top surface and for the projected image for various correlation lengths. While the size distributions for the top surface features display the expected Gaussian distribution with slight broadening for shorter correlation lengths, we find that the feature size distribution for the projected image does not replicate the top-surface distribution. For the projected-image features, the size distribution deviates from Gaussian and develops a tail toward smaller features. The median of the projected-image features also shifts to smaller values compared to those observed at the top surface. Finally, the number of transferred features is reduced considerably for shorter correlation lengths. We explain the discrepancy between the top-surface image and the projected image with a simplified tilting-cylinder model that takes into account the tilting that cylinders undergo in the vicinity of dislocations.

Out-of-plane translational order for optimal pattern transfer has significant importance for any case of block copolymer lithography, not just the fabrication of BPM. Even with directed self-assembly, where grain boundaries are eliminated and long-range in-plane translational order is achievable, a single point defect can induce tilting in nearby domains, causing a missing feature at the defect location and poor transfer at nearby locations. Systematically tilted block copolymer domains may also occur with alignment to a chemical prepattern in directed self-assembly—for example, due to domain size mismatch.[18−21] The loss of translational order in the direction out of plane limits the extent of what pattern rectification[3,4,22,23] or roughness remediation[23,24] can achieve with directed self-assembly underscoring the importance of controlling block copolymer side-wall profile for any lithographic application.

II. EXPERIMENTAL DETAILS

2.1. Block Copolymer Self Assembly. Substrates with neutral interaction to the block copolymer were created by grafting a thin layer of hydroxyl-terminated polystyrene-*ran*-poly(methyl methacrylate) M_N 8 kg/mol, 63% by mass PS onto clean silicon substrates by spin coating and annealing at 200 °C in vacuum for 12 h. Unbound material was then rinsed from the substrates with toluene immediately before block copolymer application. After rinsing, the random copolymer layer was ∼6−7 nm thick.

For the block copolymer films, we use polystyrene-block-poly(methyl methacrylate) (PS-*b*-PMMA, Polymer Source, M_N 65 kg/mol, M_W/M_N 1.07, 69% by mass PS) which self-assembles into PMMA cylindrical domains in a PS matrix. The PS-*b*-PMMA was applied by spin coating from toluene solution onto substrates with a neutral grafted layer. The cylinders form a hexagonal closed packed lattice with a center-to-center pitch of 38 nm. PS-*b*-PMMA films (∼55 nm thick) on neutral substrates were annealed in vacuum for 1 h at 190, 200, and 210 °C, and for 20 min at 220 °C. The resulting films self-assembled in cylinders of PMMA aligned perpendicular to the film, in randomly oriented crystallite grains with various correlation lengths. Correlation lengths and feature size distributions were calculated from scanning electron micrographs. SEM micrographs covered 2048 × 2048 pixels with a pixel size of 1.24 nm/pixel. Image processing and calculation of the orientational correlation length followed procedures described elsewhere.[3,25,26]

2.2. Cr Lift-off from Block Copolymer Films. As described elsewhere,[3,6] the PMMA in perpendicular cylinders was selectively degraded by exposure to UV and then removed by rinsing in acetic acid, leaving a porous PS film A subsequent reactive ion etching in oxygen plasma removes the remaining grafting layer cleaning the bottom of the pores. While doing so, the anisotropic oxygen plasma etch also removes about 20−25 nm from the top of the film. A 6 nm thick layer of Cr was

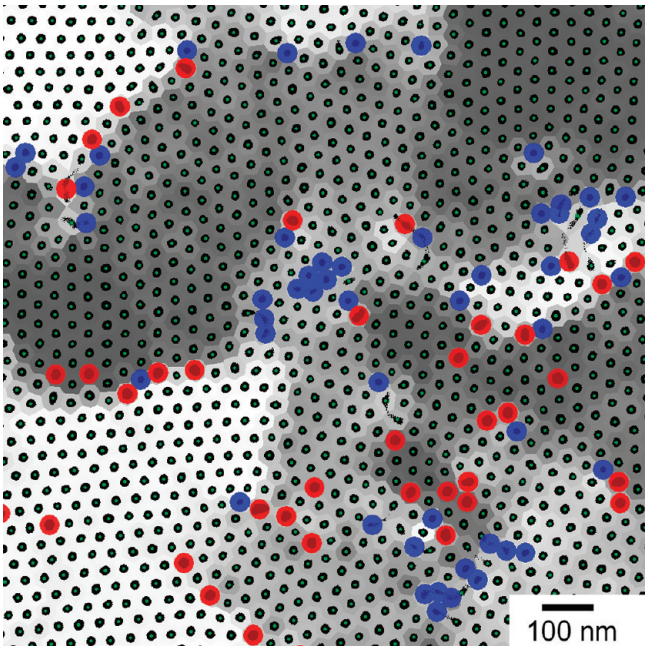

Figure 2. Processed image of the top-surface features of a block copolymer film. The black dots are the cylindrical pores. The shaded areas are an overlay of the real part of the order parameter. Different gray tones correspond to different crystallite orientations. The green points represent the location of the dot centroids. The blue dots highlight the location of features for which $a < a_{mean} - 2.5\sigma_a$. The red dots highlight the location of features for which $a > a_{mean} + 2.5\sigma_a$.

deposited using an e-beam evaporator. The remaining polystyrene film was lifted off in piranha (2:1 v/v sulfuric acid and 30% hydrogen peroxide). The Cr dots are interpreted as an approximate rendition of the two-dimensional image projected by the block copolymer cylinder cores.

III. RESULTS AND DISCUSSION

3.1. Lateral Correlation Length and Top-Surface Feature Size Uniformity. Self-assembling block copolymers undergo microphase separation when annealed at temperatures above their glass transition temperature (inducing chain mobility) but below the order−disorder temperature.[27] The cylindrical phase block copolymers used here on neutral substrates form perpendicularly oriented cylindrical domains. A view from the top or at any sliced plane parallel to the substrate reveals the generally circular cylinder cores as an array of dots in a hexagonal lattice with polycrystalline order such as the example in Figure 2. The local orientation of the lattice at any point $\vec{r}$ in the 2D plane can be quantified by the order parameter[25,28] $\psi(\vec{r}) = e^{i6\theta(\vec{r})}$ where $\theta(\vec{r})$ is the orientation of the bond between nearest neighbors obtained from Delaunay triangulation. The factor of 6 accounts for the 6-fold symmetry of the hexagonal lattice. For a sample with multiple grains, the azimutally averaged correlation function $g_6(r)$ can be approximated to an exponential function

$$g_6(r) = \langle \psi^*(\vec{0})\psi(\vec{r})\rangle_c = \exp\left[-\frac{r}{\xi}\right] \quad (1)$$

where the brackets $\langle\rangle$ denote azimuthal averaging and ξ stands for the orientational correlation length. In Figure 2 the black dots are the pores formed after selective removal of the PMMA minor phase; the background is shaded with a gray scale that corresponds to the local value of the real part of the orientational order parameter, $\psi(\vec{r}) = e^{i6\theta(\vec{r})}$. Thus, sections with the same shading have the same crystallite orientation and grain boundaries can be visualized as the intersection of two regions with different gray tones.

Self-assembled block copolymer patterns coarsen with annealing time, t, for a given annealing temperature, T, according to the power law[29,30]

$$\xi = A_T t\phi \quad (2)$$

where ϕ is the growth exponent and A_T is a temperature-dependent coefficient. Given that the correlation length is a quantity associated with the lateral size of the pattern that exhibits a single crystallographic orientation[28,31] it follows that the defect density, ρ_ε, (for defects that disrupt the orientational order) decreases as ξ increases.

Previous studies have shown that the cylindrical features inside the grains having six-nearest neighbors display a Gaussian feature size distribution.[11−13] It has also been shown that the features located at the grain boundaries (i.e., features having five or seven nearest neighbors) depart from the Gaussian distribution creating satellite distributions at both tails of the Gaussian curve, broadening the overall size distribution.[12,13] Our samples reproduce this behavior as shown in Figure 2. Features whose area a falls in the interval: $a_{mean} - 2.5\sigma_a < a < a_{mean} + 2.5\sigma_a$ are marked with green points located at the centroid of the features, those with $a > a_{mean} + 2.5\sigma_a$ are highlighted with red circles and those with $a < a_{mean} - 2.5\sigma_a$ are highlighted with blue circles. As seen in Figure 2, the majority of the anomalously sized dots are located along or within one domain spacing of the grain boundaries. The anomalously sized dots are commonly found among features with five or seven nearest neighbors. The change in domain size has been explained in the past with a two-dimensional model in which polymer features at the grain boundaries deform in response to the strain built at the defect core. While the two-dimensional model explains the variations in size for top-surface features with five or seven neighbors as seen from top-down images, we find here that the size distribution of the projected lithographic image requires more than a two-dimensional model to fully explain the structure of block copolymers throughout the thickness of the film. If these films were purely two-dimensional, the feature size distribution of the projected image should replicate that of the top-surface. If the film is three-dimensional, the discrepancy between the top-surface and projected image can be indicative of the distortions occurring inside the film.

We evaluate the evolution of both top-surface and projected-image feature size uniformity with ξ by fabricating block copolymer films with a variety of correlation lengths (and, hence, a corresponding variety of defect densities). It is possible to change ξ by changing the annealing temperature or the annealing time, but given that defect annihilation is a rather slow mechanism, we opted for using the annealing temperature as a parameter to impact the correlation length at short annealing times.[30,32] Parts a−d of Figures 3 show top-down micrographs of block copolymer films on neutral substrates that were annealed at different temperatures resulting in hexagonal arrays of perpendicularly oriented cylinders with correlation lengths of ξ = 105, 145, 187, and 194 nm respectively (the images shown are only a small portion of the overall image used in computing ξ). The corresponding histograms for the top-surface feature sizes are displayed in Figure 4a. The plots for samples with different ξ are color coded to help in visualizing them against the SEM micrographs of

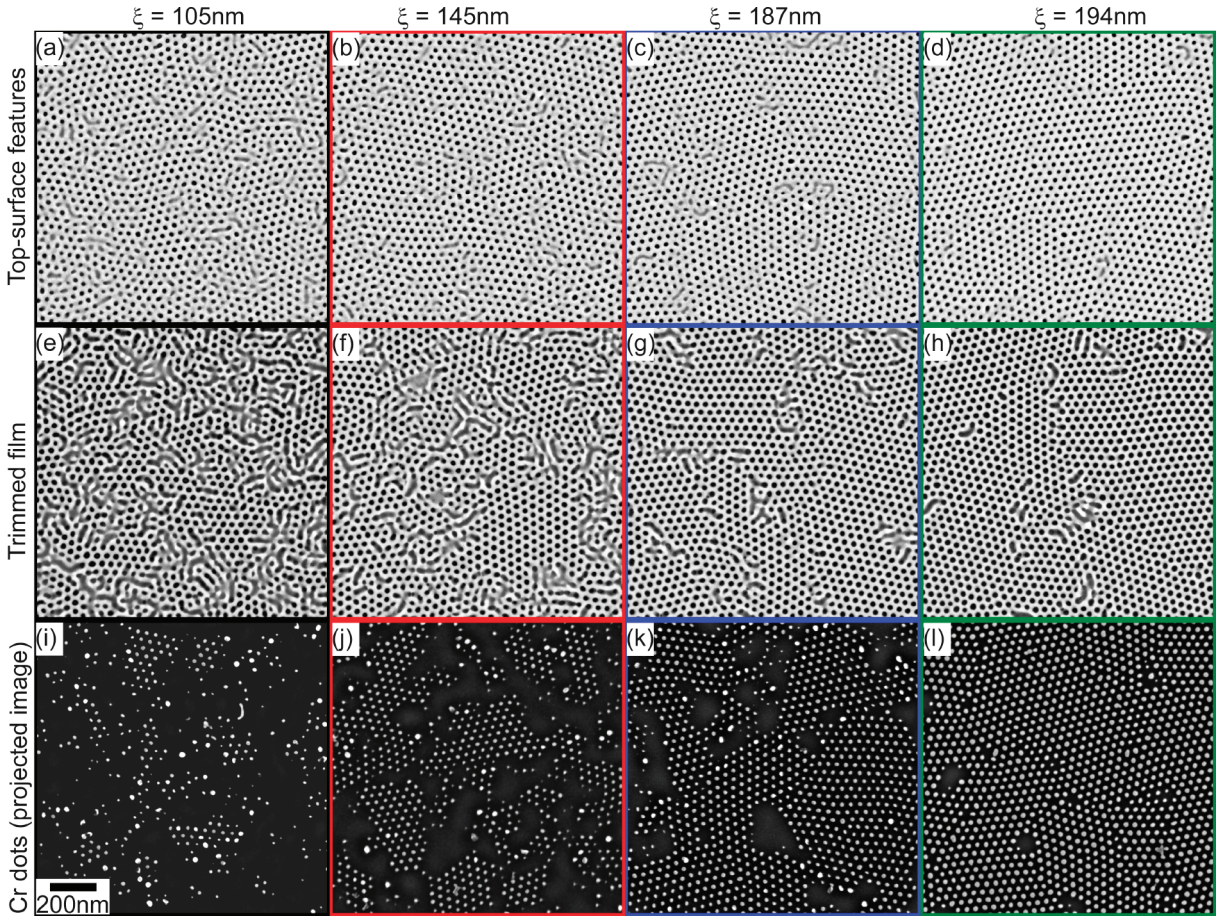

Figure 3. SEM micrographs of the top-surface features after selective removal of the PMMA cores (a−d), the trimmed film after oxygen plasma etch (e−h) and the lithographic projected-image as reproduced by Cr dots (i−l) for various correlation lengths.

Figure 3, parts a−d. The histograms are plotted as a probability density normalized against the feature density for a hexagonal lattice with lattice constant L_o. That is, the integral under the continuous curve equals: $N/(A\rho)$ where N is the total number of top-surface single dots. A is the area of the analyzed image and $\rho = 2/((3)^{1/2}L_o^2)$ is the density of features per unit area. Note that the histograms in Figure 4 correspond only to counts of single-sized features. Merged dots with area $\geq 2a_o$ are not shown in the histograms nor are they included in the value of N. Merged dots occur mostly at grain boundaries where defects are located. Rather than focusing on the topological aspects of defects at grain boundaries, in this study we want to concentrate our attention on the uniformity of the single-sized features located inside the grains and away from the grain boundaries. Hence, the histograms follow the distributions of single-sized features.

Table 1 summarizes the mean size and standard deviation for all samples. The mean size of the top-surface features is about the same for all samples, independent of correlation length. The accuracy of the size measurement is estimated to be below 1 nm in diameter.[33] The area variations in all four samples translate into diameters that are within 1 nm. The standard deviation, on the other hand, shows a small but continuous decrease with increasing correlation length. The variations in the standard deviation of the top-surface feature size reflect what was known for top-surface feature size: samples with more grain boundaries having more features with five and seven neighbors will result in broader distributions.

3.2. The Projected Image at the Substrate Interface. When using block copolymer films as lithographic masks, it is common to selectively remove one block to render a porous film. The transferred feature is a replication of the two-dimensional image that the pores project at the substrate interface. If the block copolymer patterns are two-dimensional, i.e., if the pattern does not change throughout the thickness of the film, then the projected image at the substrate interface should replicate the image at the top of the film (or at any plane parallel to the substrate within the film). The uniformity of the projected image at the substrate interface can be measured by a liftoff process. After the block copolymer film is annealed to form perpendicular cylinders, the cylindrical PMMA domains are selectively removed followed by a brief oxygen plasma treatment. The oxygen plasma cleans the remaining brush layer at the bottom of the film. While doing so, it also removes ∼20−25 nm from the top revealing the structure of the film a few nanometers below the top surface. Cr dots are formed at the substrate interface where the PMMA was previously located by depositing a 6 nm Cr film on the porous film and then lifting off the polymer mask (including the Cr coating) in piranha solution.

Parts e−h of Figure 3 show the various block copolymer films after being thinned down ∼20−25 nm by oxygen plasma. A few nanometers below the top surface, the images reveal a network of merged dots or worm-like stripes. These structures are more pronounced for shorter correlation lengths. The effect can be seen

more quantitatively in plot 4(b) where there is a significant reduction in the counts of single dots for shorter correlation lengths. The mean size after oxygen plasma in 4(b) is larger than before plasma treatment in 4(a) because the oxygen plasma also widens the pores. However, the size distributions for single dots as seen from the top remain nearly Gaussian with smaller standard deviations for larger correlation lengths (see Table 1). The worm-like stripes visible in Figure 3, parts e−h, may be indicative of the three-dimensional structure of the film. A possible explanation is to consider cylinders that are not fully perpendicular to the substrate that bend forming a network of tunnels and bridges inside the film. Trimming down the film with oxygen plasma would reveal these bent cylinders as the stripes of worm-like features in Figures 3, parts e−h. Alternatively, it is also possible that merged dots could be artificially caused by the oxygen plasma process that erodes part of the cylinder walls as it trims the film down. This however is unlikely given that the etch process used is highly anisotropic. The increase in pore diameter (∼6 nm) is much less than the average edge-to-edge distance (∼20 nm). Still dots whose edge-to-edge distance is less than 6 nm could be merged by the oxygen plasma, but as will be seen next, data after Cr liftoff supports a bent-cylinder model over a two-dimensional model.

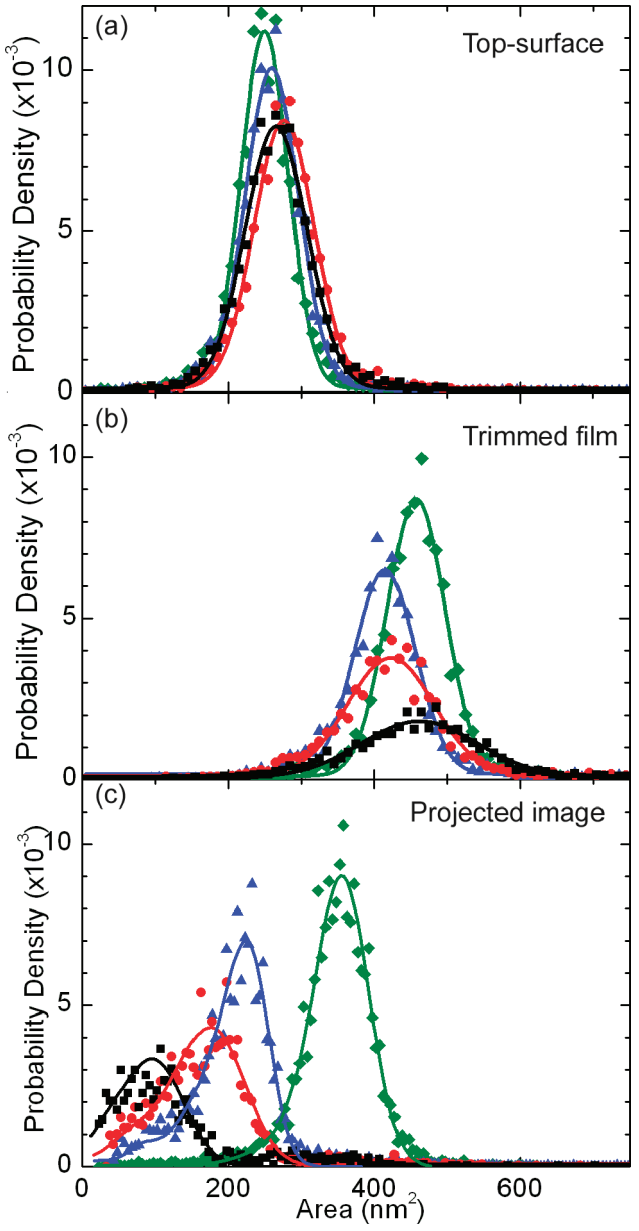

Figure 4. Size distributions for features as observed at the top-surface (a), trimmed film (b) and the projected-image as reproduced by the Cr dots (c). The color code matches that used in Figure 3: (■) ξ = 105 nm; (red ●) ξ = 145 nm; (blue ▲) ξ = 187 nm; (green ◆) ξ = 194 nm.

The features' projected image at the substrate interface replicated by Cr dots after liftoff is shown in Figure 3, parts i-l, with corresponding histograms in plot 4(c). First, we note that, for the most part, the worm-like stripes and/or merged dots did not transfer indicating that the opening did not reach the bottom of the film, i.e., it is not two-dimensional. Second, the feature size distributions showed a significant deviation from their original Gaussian shapes developing a tail on the left side of the distribution. Additionally, the distributions show a shift of the median toward smaller dimensions. The tail and shift are more pronounced for shorter correlation lengths.

The data presented in Figures 3 and 4 suggest a three-dimensional model in which cylinders bend in response to the strain near a defect core, rather than a purely two-dimensional deformation that would require a larger reduction in conformational entropy. The deformations of the otherwise perpendicular cylinders are reflected in variations both in-plane and out-of-plane. Within the plane, and as seen from the top, the deformations are appreciated as variations in feature size contributing to the slight increase in counts on both sides of the Gaussian distribution, i.e., the size distributions of the five and seven neighbor dots reported before.[12] Out of plane, the deformations result in loss of translational order in the vertical direction as the cylinders tilt, bend or oscillate throughout the thickness of the film. This also implies that the position of the two-dimensional centroids at any given plane shifts throughout the film. When looking at any given plane, the effects of cylinder deformation are seen as changes in size distribution, e.g., larger σ_a for shorter correlation lengths. When looking at the composite effect throughout the film, i.e., the projected image, the shape of the size distribution and the

Table 1. Feature Size and Standard Deviation for Top-Surface Features and after Trimming for Samples with Various Correlation Lengths, ξ (a = Area, d = Diameter)

		top surface after PMMA removal			trimmed film after O_2 RIE		
annealing temp (°C)	ξ (nm)	a_{mean} (nm^2)	$\sigma_a/\ a_{mean} \times 100$ (%)	d_{mean} (nm)	a_{mean} (nm^2)	$\sigma_a/\ a_{mean} \times 100$ (%)	d_{mean} (nm)
190	105	265	16	18.4	462	17	24.3
200	145	276	15	18.7	423	14	23.2
210	187	260	14	18.2	415	10	23
220	194	249	13	17.8	458	9	24.1

dx.doi.org/10.1021/ma201967a |*Macromolecules* 2011, 44, 9196–9204

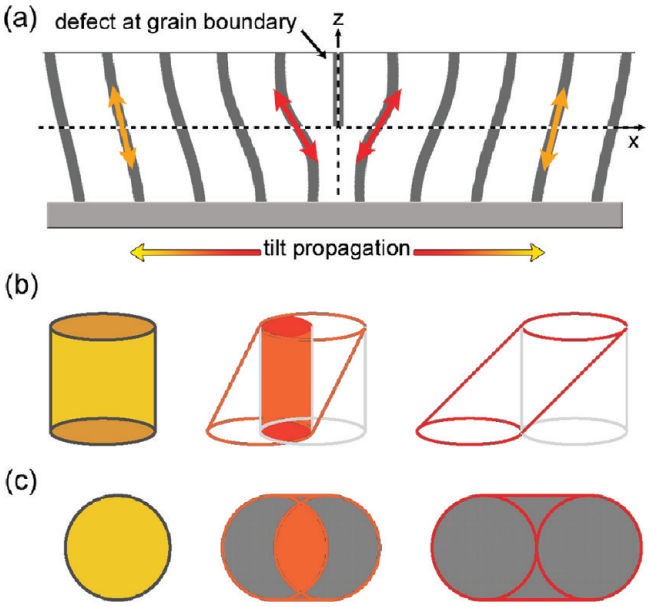

Figure 5. (a) Representation of a dislocation and the cylinder tilting around the defect core. The tilting propagates to the neighbors over some distance. (b, c) Representation of the projected image for various degrees of cylinder tilting.

location of the median also change. In lithographic applications, these deformations perturb the uniformity of the projected image at the substrate interface that ultimately produces the lithographic feature.

3.3. Modeling the Size Distribution of the Projected Image. In an attempt to understand how three-dimensional deformations around defect cores could result in projected-image size distributions like the ones shown in Figure 4c, we present a simple model that captures the basic features of shifted median, skewed distribution and missing dots based on the characteristic deformations observed around dislocation defects and the subsequent tilting that propagates to neighboring cylinders.

The area a_{cyl} of the circular cross sections of the cylindrical cores has a normal distribution, $f(a_{cyl})$ given by[11,12]

$$f(a_{cyl}) = \frac{1}{\sqrt{2\pi\sigma_a{}^2}} \exp\left[-\frac{(a_{cyl}-a_0)^2}{2\sigma_a{}^2}\right] \quad (3)$$

where a_{cyl} is the cross-sectional area of a cylinder, a_0 is the average cross-sectional cylinder area, and σ_a is the standard deviation of the cross sectional area.

Next we consider the tilting angle of a cylinder core in the vicinity of a dislocation. Figure 5 shows a representation of a simple dislocation. The cylindrical cores bend around the defect core. The tilting or deformation is more pronounced for the cylinders immediately adjacent to the dislocation core and propagates to the neighbors. Eventually the orientation of the cylinders relaxes to its vertical orientation further away from the defect core. If we use Figure 5a as a reference and locate the origin at the dislocation core with the x and z axes along the horizontal and vertical lines respectively, then the amount of tilting of a given cylinder with respect to the vertical axis is given by[17]

$$\theta(x) = \frac{b}{4\sqrt{\pi\lambda x}} \exp\left[-\frac{z^2}{4\lambda x}\right] \quad (4)$$

where θ is the cylinder tilt angle from normal at distance x from the defect; b is the Burger's vector, here $b = L_o$; and λ is defined as:

$$\lambda = \sqrt{\frac{k_1}{B}} \approx L_o \quad (5)$$

where k_1 is the splay elastic modulus for the polymer and B is the Young's modulus. Typically, $\lambda \approx L_o$.[17] eq 4 shows that the tilt deviation propagates from the defect, with large value near the defect and smaller value away from the defect.

In our model, we make several assumptions to simplify the analytical expression. The first is that all crystallite grains are circular with radius R_0 and that R_0 scales with ξ. We only consider dislocation defects with Burgers vector $b = L_o$ (i.e., one lattice constant). All defects are presumed to be located at grain boundaries. Thus, we assume that a cylinder's tilt angle is dependent on its radial position r, which is a distance $(R_0\text{-}r)$ from the grain boundary. We simplify the distortion around the defect core to be a simple tilting with a constant tilting angle along the vertical direction as shown in Figure 5b. We take θ in eq 4 for the case when $z = 0$. Thus, we alter eq 4 to reflect distance from the grain boundary:

$$\theta(R_0 - r) = \frac{b}{4\sqrt{\pi\lambda(R_0 - r)}}; \quad \text{for } 0 \le \theta(R_0 - r) \le 2\pi \quad (6)$$

We understand that the assumptions made above represent an oversimplification of the actual arrangements of the block copolymer cylinders in our films, especially because we only consider simple dislocations of Burgers vector $b = L_o$ which may not be enough to explain the large worm-like features observed inside the film around the grain boundaries as shown in Figure 3, parts e−g. Larger Burgers vectors or other types of defects such as disclinations may need to be included to reflect such observations. In any case, all of these defects will induce cylinder tilting in nearby cylinders. Our main goal is to provide a first order approximation to explain the effect that cylinder tilting may have on the uniformity of the features projected at the substrate interface and away from the grain boundaries which are commonly used for lithographic applications.

From now on, we use θ to refer to $\theta(R_0 - r)$ for simplicity. Figure 6a shows a map for the tilting angle, θ, as given in eq 6 for a single crystal grain with $R_o = 200$ nm. The color map shows that cylinders near the grain boundary have a pronounced tilting angle whereas those at the center are nearly vertical. It is easy to see also that if a grain is not sufficiently large, the tilting angle does not have enough space toward the center of the grain to relax; even cylinders at the center could have significant tilting. Therefore, samples with short R_o (and hence short ξ) would have a larger fraction of their overall cylinders with considerable tilting.

As mentioned above, we assume that the tilted cylinders are straight cylindrical shapes with simple tilting, not curved nor bent, and that their cross sectional area (as measured in a plane parallel to the substrate) remains constant throughout the film. In other words, we replace the deformed cylinders of Figure 5a by straight tilted cylinders like the ones shown on Figure 5b. The projected image area at the bottom of the film is given by the overlap of the cross sectional areas of the cylinder at the top and bottom interfaces as in Figure 5c. A tilted cylinder would have ellipsoidal cross sectional areas in a plane parallel to the substrate. However, to simplify the mathematical expression, we approximate the projected area onto the substrate as the overlap of two discs of equal area (corresponding to the top and bottom of the cylinder) with a separation distance determined by the tilt angle

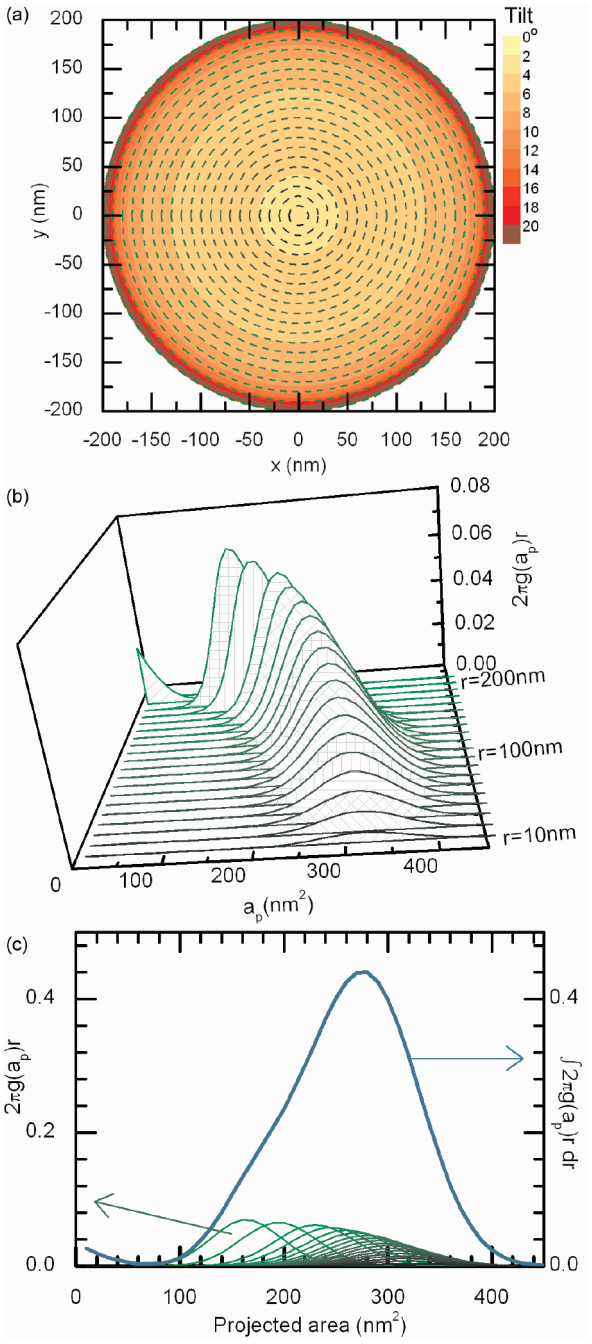

Figure 6. (a) Map of the cylinder tilting angle as a function of the radial position inside the grain. (b) Size distribution histograms for the projected-image for various radii. Near the grain boundary, the distribution of the projected image shifts to smaller values due to cylinder tilting. (c) Overall projected-image size distribution over the entire grain.

(θ) and film thickness (h) as shown in Figure 4c. With these assumptions, the area of the projected image, a_p, is defined:

$$a_p = \frac{2a_{cyl}}{\pi}\cos^{-1}\left(\frac{h}{2}\sqrt{\frac{\pi}{a_{cyl}}}(\tan\theta)\right) - h\tan\theta\sqrt{\frac{a_{cyl}}{\pi} - \frac{h^2}{4}(\tan\theta)^2};$$

$$\text{for } a_{cyl} > 0,\ 0 \le \theta < \frac{\pi}{2},\ \text{and } 0 \le \frac{h}{2}\sqrt{\frac{\pi}{a_{cyl}}}(\tan\theta) \le 1 \qquad (7)$$

We see that $a_p < a_{cyl}$ when the tilt angle deviates from the normal. Because θ is a function of distance from the grain boundary, i.e., $\theta(R_0 - r)$, the ratio a_p/a_{cyl} also displays a radial dependence: the ratio is largest at the center of the grain and smaller (and eventually zero) near the edges. If the cylinder is sufficiently tilted (nearest the grain boundary), the projected area is zero and results in a missing projected dot. Equation 7 also shows the dependence that a_p has on h. Lithographically, a thinner film would be desirable to achieve maximum fidelity since $a_p \rightarrow a_{cyl}$ as $h \rightarrow 0$. On the other hand, the porous polymer film must be sufficiently thick for a good liftoff or any other pattern transfer process. Therefore, eq 6 highlights the importance of finding the minimum necessary film thickness for a given lithographic process.

For a given a_o, r, R_0, and h, it is possible to calculate back the value of a_{cyl} given a_p by defining an inverse function $INV[a_p(r, R_o, h)]$:

$$a_{cyl} = INV[a_p(r, R_o, h)] \quad \text{for } a_p > 0,\ 0 \le \theta < \frac{\pi}{2},$$

$$\text{and } 0 \le \frac{h}{2}\sqrt{\frac{\pi}{a_{cyl}}}(\tan\theta) \le 1 \qquad (8)$$

We note that a_p in eq 7 is monotonic within the defined range and thus a_{cyl} in eq 8 is single-valued. The inverse function can be computed numerically by first constructing a grid using eq 7. The inverse function for a_{cyl} can then be solved by interpolation using the grid.

We recall from eq 3 that the cylinder areas (or pores, after removal of the material in the cylinders) follow a Gaussian distribution function, $f(a_{cyl})$. Using eqs 3 and 8, it is possible to obtain an expression for the size distribution, $g(a_p, r, R_o, h)$, of the projected image by substituting eq 8 into eq 3:

$$g(a_p, r, R_0, h) = f(INV[a_p(r, R_o, h)]) \qquad (9)$$

At a given radius, r, within a single crystal grain, the perimeter-weighed product $2\pi r \cdot g(a_p, r, R_o, h)$ represents the histogram of the projected image for all cylinders located at r. Figure 6(b) shows the histograms $2\pi r \cdot g(a_p, r, R_o, h)$ for various radii within a grain. To generate the plot, $a_o = 400$ nm^2, $\sigma_a = 50$ nm^2 and $h = 55$ nm were used as the average cylinder cross sectional area, standard deviation and film thickness, respectively. The tilting angle is given by eq 6. The radii positions for the various examples in Figure 6b are highlighted with dashed lines in part a to help in visualizing the tilting angle effect on $g(a_p, r, R_o, h)$. Looking at the plot in part b, for small r, far from the dislocations, the median size of a_p is close to a_o. For larger r, and closer to the dislocations where the cylinders tilt more, the median of a_p shifts to smaller values until eventually the distribution is cut off due to sufficiently large tilting where a_p vanishes. The histograms for larger radii have a higher amplitude (i.e., more counts) due to the weighing factor $2\pi r$. This is simply because a larger perimeter can accommodate more features than smaller ones for a constant density.

The final probability density function $G(a_p, R_o)$ for the projected image area is obtained from the integration of $g(a_p, r, R_o, h)$ over the entire grain area

$$G(a_p, R_0) = \frac{1}{\pi {R_0}^2 \rho}\int_0^{R_0} 2\pi\rho g(a_p, r, R_0, h) r\, dr \qquad (10)$$

dx.doi.org/10.1021/ma201967a |*Macromolecules* 2011, 44, 9196–9204

Table 2. Results for the Fitting Parameters R_o, a_o, σ_a, and h for Samples with Various Correlation Lengths

ξ (nm)	R_o (nm)	a_o (nm^2)	σ_a (nm^2)	h (nm)
105	79.5	241.6	44.4 (18.4%)	58.9
145	112.3	309.6	44.6 (14.4%)	53.3
187	214	318.7	26.5 (8.3%)	51.6
194	589.5	397.6	35.4 (8.9%)	27.5

where ρ is the feature density:

$$\rho = \frac{2}{\sqrt{3}L_0^2} \tag{11}$$

Figure 6c shows again the various sample plots of $2\pi r \cdot g(a_p, r, R_o, h)$ used in 6(b). The integral, or continuous summation, over all r is shown in blue plotted against the right axis. The integral in eq 10 represents now the final histogram for the projected image of all features in the grain. This final distribution has the same attributes seen in our liftoff data, namely, the distribution is no longer Gaussian, the median size is smaller than a_o and the overall distribution has a tail toward smaller feature dimensions. From the plots in Figure 6c, we see that the shift in median value and the tail to the left of the distribution arise from the corresponding shift of the median of $g(a_p, r, R_o, h)$ and the perimeter weight factor.

3.4. Predicting Pattern Transfer Using the Tilted Cylinder Model. We used eq 10 to best-fit the size distribution histograms of transferred Cr dots (Figure 4c) to compare the experimental data against the simplified model presented here. The fitting parameters are R_0, h, a_0, and σ_a. The fitted curves are the continuous lines shown in Figure 4c. The fitted parameters in Table 2 show a trend according to the actual values listed in Table 1. The fitted curves captured the attributes of our data such as the shift in median values the tails toward the left part of the distribution and total number of transferred dots. There are some discrepancies with the experimental data that may arise from the oversimplification of the model. For example, the model assumes that the crystallite grains are round and identical in size. It is also assumed that the cylinders are tilted, but straight, with no bending. We are also not including cylinder roughness or undulations that may become more dominant in very thick films. Finally, the sample with ξ = 194 nm may have a larger correlation length, but the measurement could be limited by size effects that limit the measurement when the *image size* is below $\sim 10\xi$.

The normalization factor in eq 10 ensures that the area under the curve of $G(a_p, R_o)$ represents the total fraction of transferred dots, $P(R_o)$, for a sample with a grain size R_o:

$$P(R_0) = \int_0^\infty G(a_p, R_0)\, da_p \tag{12}$$

Consequently, $1 - P(R_o)$, represents the fraction of missing dots that were not transferred due to excessive cylinder tilting. Figure 7 shows the fraction of transferred dots in our data compared to the fraction of transferred dots predicted by the fitted model. Here, the model also captures the trend of the experimental data with increasing fraction of transferred dots with increasing ξ.

The simple model proposed here captures the main attributes observed in the projected lithographic image as measured with a Cr liftoff process suggesting that block copolymer features are three-dimensional and that the deformations that result in response to the strain around defect cores are three-dimensional.

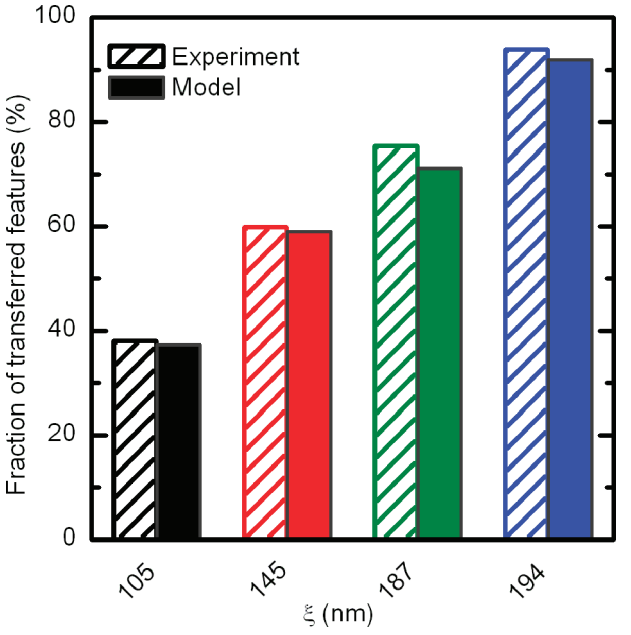

Figure 7. Comparison of the total fraction of transferred features with the value predicted by the model used to fit the data.

IV. SUMMARY

The fidelity of a lithographic feature created by block copolymer cylindrical domains derives from the quality of the two-dimensional image that the cylindrical domain projects onto the substrate. Although sometimes it is convenient to regard these patterns as two-dimensional, it is their three-dimensional structure that ultimately limits pattern transfer fidelity in lithographic applications. Any loss of translational order in the direction out of plane deteriorates the projected feature at the substrate interface. In the vicinity of defects, the cylinders deform and tilt in response to the strain built around a defect core. The deformations propagate away from the defect core with the tilting angle relaxing back to the vertical orientation for cylinders located far from the defect core. The lithographic image projected by a tilted cylinder is smaller than the corresponding two-dimensional feature seen at the top of the film. We have created a set of samples with various lateral correlation lengths, and therefore, with various defect densities. We captured the size distributions of the projected lithographic images by means of a Cr lift-off process. While the top-surface feature size shows a nearly Gaussian distribution for all samples, the projected image histograms deviate from a Gaussian distribution with a pronounced tail toward small feature dimensions and a shift of the median value. These attributes are more pronounced for samples with shorter correlation lengths.

We developed a simplified model that incorporates the degree of tilting observed near dislocations to explain the observed distributions in the lithographic features. The model captures the main characteristics observed in our data such as the shift in the size of the median, the tail in the distribution and the total amount of transferred dots suggesting that indeed there is a three-dimensional structure to these cylinders that correlates with ξ. Although most lithographic applications rely on some form of directed self-assembly to eliminate grain boundaries, the study

here suggests that any loss of translational order in the direction out of plane can damage the fidelity of the pattern transfer. Now that directed self-assembly has established itself as the best method to achieve lateral translational order in block copolymer films, the next challenge may come in controlling translational order in the direction out of plane.

AUTHOR INFORMATION

Corresponding Author

*E-mail: ricardo.ruiz@hitachigst.com.

ACKNOWLEDGMENT

We thank Greg Breyta of IBM Almaden for synthesizing PS-*r*-PMMA−OH. We thank Byron Lengsfield of Hitachi GST for helpful advice in numerical methods.

REFERENCES

(1) Segalman, R. A. *Mater. Sci. Eng., Res.* **2005**, *48* (6), 191–226.

(2) Black, C. T.; Ruiz, R.; Breyta, G.; Cheng, J. Y.; Colburn, M. C.; Guarini, K. W.; Kim, H.-C.; Zhang, Y. *IBM J. Res. Dev.* **2007**, *51* (5), 605–633.

(3) Ruiz, R.; Kang, H.; Detcheverry, F. A.; Dobisz, E.; Kercher, D. S.; Albrecht, T. R.; de Pablo, J. J.; Nealey, P. F. *Science* **2008**, *321* (5891), 936–939.

(4) Yang, X. M.; Wan, L.; Xiao, S. G.; Xu, Y. A.; Weller, D. K. *ACS Nano* **2009**, *3* (7), 1844–1858.

(5) ITRS International Technology Roadmap for Semiconductors. 2010 Edition. Lithography. http://www.itrs.net/Links/2010ITRS/Home2010.htm

(6) Hellwig, O.; Bosworth, J. K.; Dobisz, E.; Kercher, D.; Hauet, T.; Zeltzer, G.; Risner-Jamtgaard, J. D.; Yaney, D.; Ruiz, R. *Appl. Phys. Lett.* **2010**, *96* (5), 052511.

(7) Stipe, B. C.; Strand, T. C.; Poon, C. C.; Balamane, H.; Boone, T. D.; Katine, J. A.; Li, J.-L.; Rawat, V.; Nemoto, H.; Hirotsune, A.; Hellwig, O.; Ruiz, R.; Dobisz, E.; Kercher, D. S.; Robertson, N.; Albrecht, T. R.; Terris, B. D. *Nat. Photon* **2010**, *4* (7), 484–488.

(8) Albrecht, T.; Hellwig, O.; Ruiz, R.; Schabes, M.; Terris, B. D.; Wu, X. Z. Bit Patterned Magnetic Recording. In *Nanoscale Magnetic Materials and Applications*, 1st ed.; Liu, J. P., Fullerton, E. E., Gutfleisch, O., Sellmyer, D., Eds.; Springer Verlag: Berlin, 2009.

(9) Cheng, J. Y.; Sanders, D. P.; Truong, H. D.; Harrer, S.; Friz, A.; Holmes, S.; Colburn, M.; Hinsberg, W. D. *ACS Nano* **2010**, *4* (8), 4815–4823.

(10) Liu, C. C.; Nealey, P. F.; Raub, A. K.; Hakeem, P. J.; Brueck, S. R. J.; Han, E.; Gopalan, P. *J. Vac. Sci. Technol. B* **2010**, *28* (6), C6B30–C6B34.

(11) Guarini, K. W.; Black, C. T.; Yeuing, S. H. I. *Adv. Mater.* **2002**, *14* (18), 1290.

(12) Hammond, M. R.; Sides, S. W.; Fredrickson, G. H.; Kramer, E. J.; Ruokolainen, J.; Hahn, S. F. *Macromolecules* **2003**, *36* (23), 8712–8716.

(13) Xiao, S. G.; Yang, X. M. *J. Vac. Sci. Technol. B* **2007**, *25* (6), 1953–1957.

(14) Welander, A. M.; Nealey, P. F.; Cao, H.; Bristol, R. *J. Vac. Sci. Technol. B* **2008**, *26* (6), 2484–2488.

(15) Stuen, K. O.; Thomas, C. S.; Liu, G. L.; Ferrier, N.; Nealey, P. F. *Macromolecules* **2009**, *42* (14), 5139–5145.

(16) Ji, S. X.; Liu, C. C.; Liao, W.; Fenske, A. L.; Craig, G. S. W.; Nealey, P. F. *Macromolecules* **2011**, *44* (11), 4291–4300.

(17) Kleman, M.; Lavrentovich, O. D. *Soft Matter Physics. An Introduction*; Springer-Verlag: New York, 2003.

(18) Edwards, E. W.; Muller, M.; Stoykovich, M. P.; Solak, H. H.; de Pablo, J. J.; Nealey, P. F. *Macromolecules* **2007**, *40* (1), 90–96.

(19) Liu, G. L.; Delcambre, S. P.; Stuen, K. O.; Craig, G. S. W.; De Pablo, J. J.; Nealey, P. F.; Nygard, K.; Satapathy, D. K.; Bunk, O.; Solak, H. H. *J. Vac. Sci. Technol. B* **2010**, *28* (6), C6B13–C6B19.

(20) Nagpal, U.; Kang, H.; Craig, G. S. W.; Nealey, P. F.; de Pablo, J. J. *ACS Nano* **2011**, *5* (7), 5673–5682.

(21) Detcheverry, F. A.; Liu, G. L.; Nealey, P. F.; de Pablo, J. J. *Macromolecules* **2010**, *43* (7), 3446–3454.

(22) Tada, Y.; Akasaka, S.; Takenaka, M.; Yoshida, H.; Ruiz, R.; Dobisz, E.; Hasegawa, H. *Polymer* **2009**, *50* (17), 4250–4256.

(23) Cheng, J. Y.; Rettner, C. T.; Sanders, D. P.; Kim, H.-C.; Hinsberg, W. D. *Adv. Mater.* **2008**, *20* (16), 3155–3158.

(24) Stoykovich, M. P.; Daoulas, K. C.; Muller, M.; Kang, H. M.; de Pablo, J. J.; Nealey, P. F. *Macromolecules* **2010**, *43* (5), 2334–2342.

(25) Segalman, R. A.; Hexemer, A.; Hayward, R. C.; Kramer, E. J. *Macromolecules* **2003**, *36* (9), 3272–3288.

(26) Harrison, C.; Anglescu, D. E.; Trawick, M. L.; Cheng, Z.; Huse, D. A.; Chaikin, P. M.; Vega, D. A.; Sebastian, J. M.; Register, R. A.; Adamson, D. H. *Europhys. Lett.* **2004**, *67*, 800–806.

(27) Bates, F. S.; Fredrickson, G. H. *Annu. Rev. Phys. Chem.* **1990**, *41* (1), 525–557.

(28) Harrison, C.; Angelescu, D. E.; Trawick, M.; Cheng, Z. D.; Huse, D. A.; Chaikin, P. M.; Vega, D. A.; Sebastian, J. M.; Register, R. A.; Adamson, D. H. *Europhys. Lett.* **2004**, *67* (5), 800–806.

(29) Harrison, C.; Cheng, Z.; Sethuraman, S.; Huse, D. A.; Chaikin, P. M.; Vega, D. A.; Sebastian, J. M.; Register, R. A.; Adamson, D. H. *Phys. Rev. E* **2002**, *66* (1), 011706.

(30) Ruiz, R.; Bosworth, J. K.; Black, C. T. *Phys. Rev. B* **2008**, *77* (5), 054204.

(31) Segalman, R. A.; Hexemer, A.; Kramer, E. J. *Phys. Rev. Lett.* **2003**, *91* (19), 196101.

(32) Welander, A. M.; Kang, H. M.; Stuen, K. O.; Solak, H. H.; Muller, M.; de Pablo, J. J.; Nealey, P. F. *Macromolecules* **2008**, *41* (8), 2759–2761.

(33) Ho, C. S. *IEEE Trans. Pattern Anal. Machine Intelligence* **1983**, *5* (6), 593–601.